A Coupled Inviscid-Viscous Airfoil Analysis Solver, Revisited*

Krzysztof J. Fidkowski [†]

University of Michigan, Ann Arbor, MI 48109

This paper presents a self-contained, comprehensive exposition and new elements of a classic airfoil analysis technique: an integral boundary layer solver coupled to a vortex-panel potential-flow method. The resulting solver mfoil, implemented in Matlab and made freely available, builds on the XFOIL code and documentation, which serve as the inspiration, reference, and standard of comparison. Modifications made in the present implementation include an augmented-state coupled solver for more control in limiting the state update, a new stagnation-point formulation to reduce leading-edge oscillations in the boundary layer variables, and a more robust treatment of the amplification rate near transition. Several results highlight these modifications and demonstrate capabilities of the code.

Nomenclature

c	=	airfoil chord length
c_{air}	=	speed of sound
c_d	=	drag coefficient
c_D	=	dissipation coefficient, $1/(\rho_e u_e^3) \int \tau(\partial u/\partial \eta)d\eta$
c_f	=	skin-friction coefficient, $2\tau_{\text{wall}}/(\rho_e u_e^2)$
c_τ	=	shear stress coefficient, $\tau_{\text{max}}/(\rho_e u_e^2)$
c_ℓ	=	lift coefficient
c_m	=	moment coefficient
c_p	=	pressure coefficient
d_i	=	edge velocity direction factor on node i
H_0	=	stagnation enthalpy
H	=	shape parameter, δ^*/θ
H_k	=	kinematic shape parameter, H computed with $\rho = 1$
H^*	=	kinetic energy shape parameter, θ^*/θ
H^{**}	=	density shape parameter, δ^{**}/θ
H^w	=	wake shape parameter, h^w/θ

---

†Professor, Aerospace Engineering, kfid@umich.edu, AIAA Associate Fellow

h^w	=	wake gap/dead-air thickness
$\hat{i}, \hat{k}$	=	unit direction vectors along x, z
m	=	mass (area) flow
M	=	Mach number
$\tilde{n}$	=	amplification factor for transition
r_{Su}	=	Sutherland's law temperature ratio
Re	=	chord-based Reynolds number, $\rho_\infty V_\infty c / \mu_\infty$
Re_θ	=	local momentum-thickness Reynolds number, $\rho u_e \theta / \mu$
s	=	arc-length distance on airfoil and wake
s_{stag}	=	stagnation point s value
$\text{Su}(\cdot)$	=	Sutherland's law function
T	=	temperature
$\mathbf{u}$	=	boundary-layer state vector
u_e	=	boundary-layer edge velocity
U_s	=	normalized wall slip velocity
u_q	=	equilibrium value of $(1/u_e) du_e/d\xi$
V_∞	=	free-stream speed
$\vec{x}$	=	spatial coordinate, $x\hat{i} + z\hat{k}$
α	=	angle of attack
γ	=	vortex sheet strength
γ_{air}	=	ratio of specific heats for air
δ	=	combined momentum and displacement thickness
δ^*	=	displacement thickness, $\int [1 - (\rho u)/(\rho_e u_e)]\, d\eta$
δ^{**}	=	density thickness
θ	=	momentum thickness, $\int (\rho u)/(\rho_e u_e)[1 - u/u_e]\, d\eta$
θ^*	=	kinetic energy thickness, $\int (\rho u)/(\rho_e u_e)[1 - u^2/u_e^2]\, d\eta$
μ	=	dynamic viscosity
ξ	=	surface distance from leading edge
ρ	=	density
σ	=	source sheet strength
τ	=	shear stress
Ψ	=	streamfunction
ω	=	Newton-Raphson under-relaxation factor

I. Introduction

The XFOIL code [1] has dominated airfoil analysis and design for over thirty years. It has been used in the design of airfoils for wind turbines [2–4], small UAVs [5, 6], marine turbines [7], aeroacoustics [8], and other applications. It has also been wrapped in scripts for analysis/design frameworks [9], and its methods have been ported to academic [10, 11] and industry codes [12]. The original publication has over 2400 citations.

Developed at a similar time as the ISES code [13–15], now a part of MISES, which features an Euler method for the outer flow, the panel code XFOIL shares the same integral boundary layer (IBL)

formulation. Compared to ISES, XFOIL cannot be applied to transonic flow, but it is simpler, faster, more robust, and easier to use. It also includes a compressibility correction that extends its domain of applicability beyond very low speeds. It is neither the first nor the only coupled inviscid/viscous airfoil analysis and design code. Other early codes include GBK [16], Eppler's PROFILE [17, 18], and GRUMFOIL [19]. However, XFOIL rose above these in adoption and longevity, for various reasons. Mathematically, its global Newton solver offers unprecedented robustness for a difficult, tightly-coupled inviscid-viscous problem. Moreover, it features a powerful user interface, built-in geometry manipulation and inverse-design capabilities, and tuned correlations for turbulence and transition. It is easily accessible, either via source code or pre-compiled versions for various platforms. Finally, it is written in optimized Fortran, so that run time is rarely an issue.

While still dominant, XFOIL is arguably feeling its age, particularly for education and even research purposes. Non-intuitive aspects for new users include a text-based menu-driven user interface, file-based input-output, and postscript graphics. Installation and run-time issues related to graphics and permissions are beginning to creep up on newer platforms. As a result, the code is becoming more difficult to use as an educational or research tool. Moreover, the epitome of a black-box code, XFOIL hides many gems, including solver tricks and undocumented models from years of tuning and modifications. These will fall by the wayside if the code stops being widely used. Herein lies the two-fold motivation for this work: (1) to distill and document the models and methods of the XFOIL code; and (2) to provide a modular and accessible enhanced implementation in a newer software environment. In addition, several modifications that enhance performance and robustness are presented.

The resulting code, mfoil [20], is written in Matlab [21] and made for both education and research. Given today's availability of computational power, speed and efficiency are not primary concerns for a two-dimensional panel/boundary-layer code. Instead, the present implementation focuses on clarity, modularity, and robustness. The code can undoubtedly be reformulated and optimized from its present version, and ported to other languages such as Python, given the modularity of the implementation. The mfoil code is a single-file Matlab class, easily searchable with all variables and methods documented and exposed to the user. It therefore supports prospects of new developments, e.g. data-driven models, adaptation, or pulling out pieces, such as the boundary-layer treatment, for other codes. It also includes new contributions: an improved stagnation-point treatment, a consistent airfoil/wake source-panel interface, smooth model functions for better convergence and optimization prospects, an augmented-state nonlinear system, a modified amplification factor growth perturbation near transition, and an angle-of attack continuation solution strategy. The remainder of this paper presents a complete description of the code and the new elements.

II. Equations and Discretization

The velocity field, $\vec{v}(\vec{x})$ in incompressible and irrotational flow satisfies $\nabla \cdot \vec{v} = 0$ and $\nabla \times \vec{v} = \vec{0}$, respectively. A velocity potential $\Phi(\vec{x})$ models irrotational velocity fields via $\vec{v} = \nabla\Phi$, and, in two dimension, a streamfunction $\Psi(\vec{x})$ models incompressible velocity fields via $\vec{v} = \nabla \times (\nabla\Psi)$. In a flow that is both incompressible and irrotational, the velocity potential and streamfunction satisfy Laplace's equation, $\nabla^2\Phi = \nabla^2\Psi = 0$. A general potential flow can therefore be modeled by superimposing elementary solutions to Laplace's equations, which include vortex and source distributions. Placing these distributions on panels in two dimensions yields a potential flow panel method for modeling the entire flowfield [22].

High-Reynolds number, subcritical flow over an airfoil can be modeled by a superposition of a constant freestream, vortex sheets, and source sheets that account for viscous displacement effects of the non-potential flow boundary layer. The present discretization follows that of [1]: $N - 1$ panels form the airfoil, and $N_w - 1$ panels form the wake, as shown in Figure 1. Global unknowns are stored at the total $N + N_w$ nodes, ordered clockwise with the wake extending the upper surface.
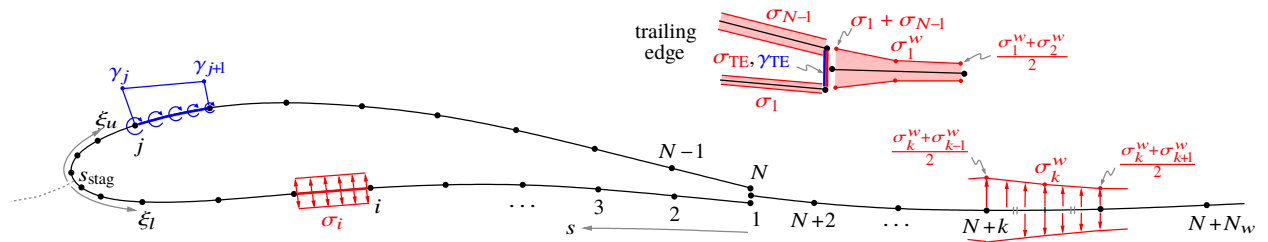

Fig. 1 **Discretization of the airfoil and wake into panels with associated placements of vortex and source sheets.**

Each panel on the airfoil contains a linear vortex sheet and a constant source sheet. Wake panels contain only source sheets, which are linear over each half-panel to avoid singular velocities at wake nodes. No such problem exists at airfoil nodes, where only streamfunction evaluations are needed. The source strength at the first wake node is the sum of the first and last airfoil panel source strengths in order to avoid a velocity spike at the trailing edge. To avoid a similar problem at the end of the wake, the last wake half panel is duplicated past node $N + N_w$, resulting in a constant-source panel with the node in the center. A constant source and linear vortex panel spans the trailing-edge gap.

III. Inviscid Formulation

For a given distribution of sources on the airfoil and wake, the requirement of flow tangency on the airfoil uniquely determines the vortex strengths. Flow tangency implies a constant streamfunction, presently enforced at the airfoil nodes. The streamfunction at an arbitrary point $\vec{x} = x\hat{i} + z\hat{k}$ in the

domain is

$$\Psi(\vec{x}) = \underbrace{V_\infty(z\cos\alpha - x\sin\alpha)}_{\Psi^\infty(\vec{x})=\text{freestream contribution}} + \sum_{k=1}^{N-1}\underbrace{\left(\mathbf{\Psi}_k^\gamma(\vec{x})[\gamma_k,\gamma_{k+1}]^T + \mathbf{\Psi}_k^\sigma(\vec{x})\sigma_k\right)}_{\text{airfoil panel } k}$$
$$+ \sum_{k=1}^{N_w-1}\underbrace{\left(\mathbf{\Psi}_k^w(\vec{x})[\sigma_{k-1}^w,\sigma_k^w,\sigma_{k+1}^w]^T\right)}_{\text{wake panel } k} + \underbrace{\mathbf{\Psi}^{\text{TE}}(\vec{x})[\gamma_N,\gamma_1]^T}_{\text{TE gap panel}} \tag{1}$$

On a wake panel, the source strength varies piecewise linearly on the two panel halves, as shown in Figure 1 and denoted by k^- and k^+, so that wake panel k contributes

$$\mathbf{\Psi}_k^w(\vec{x})[\sigma_{k-1}^w,\sigma_k^w,\sigma_{k+1}^w]^T = \mathbf{\Psi}_{k^-}^\sigma\left[\frac{1}{2}(\sigma_{k-1}^w+\sigma_k^w),\sigma_k^w\right] + \mathbf{\Psi}_{k^+}^\sigma\left[\sigma_k^w,\frac{1}{2}(\sigma_k^w+\sigma_{k+1}^w)\right] \tag{2}$$

The appendix provides expressions for the vortex and source panel streamfunction influence coefficients that appear in these two equations. In the presence of a trailing-edge gap, a constant source panel of strength $\sigma_{\text{TE}} = \frac{1}{2}(\gamma_N - \gamma_1)|\hat{t}_{\text{TE}} \times \hat{p}_{\text{TE}}|$, and a constant vortex panel of strength $\gamma_{\text{TE}} = \frac{1}{2}(\gamma_N - \gamma_1)\hat{t}_{\text{TE}} \cdot \hat{p}_{\text{TE}}$, where $\hat{t}_{\text{TE}}$ is the unit trailing-edge bisector vector and $\hat{p}_{\text{TE}}$ is the unit vector along the TE panel from node N to node 1, ensure no net flow through the gap and smooth streamlines off the upper and lower surfaces [1], as shown in Figure 2. $\mathbf{\Psi}^{\text{TE}}(\vec{x})$ accounts for the contributions of both of these TE panels.

(a) No source or vortex panel   (b) Only source panel   (c) Both source and vortex panels
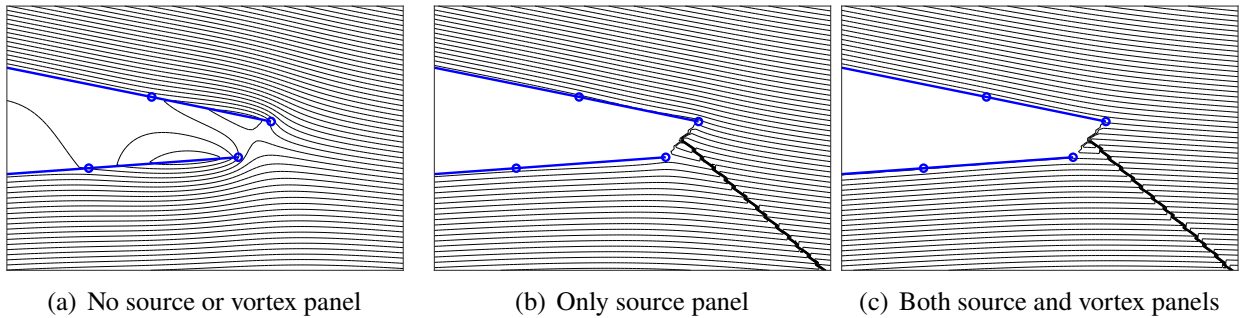
Fig. 2 Effect of trailing-edge source and vortex panels on flow near the trailing edge. The branch cut perpendicular from the constant-source panel creates the concentration of streamlines in (b) and (c).

Both the linear vortex and constant source panels have bounded streamfunction values at the panel endpoints. Constant source panels exhibit branch cuts across which the streamfunction is discontinuous. Making the cuts point outward from the airfoil on each panel prevents the discontinuities from affecting the streamfunction calculation at the airfoil nodes, as illustrated in Figure 3.

(a) Panel-aligned branch cuts (incorrect ψ) (b) Panel-perpendicular branch cuts (correct ψ)
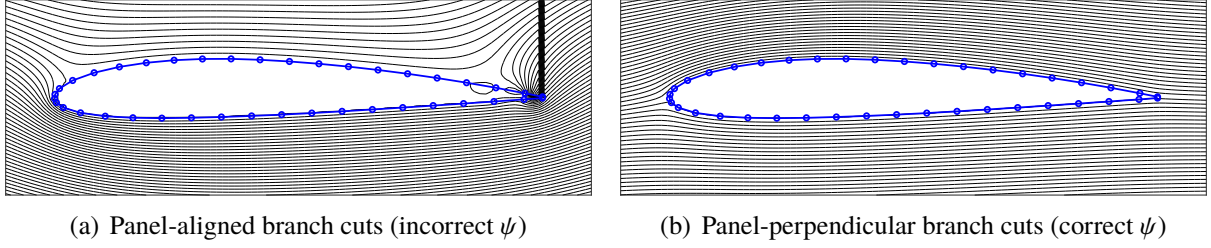
Fig. 3 Use of a standard arctangent in panel-aligned coordinates causes branch cuts of constant-source panels, here only across the trailing-edge gap, to interfere with the streamfunction calculation on airfoil nodes. Panel-perpendicular cuts, obtained by a simple shift of streamfunction values, prevent this problem.

Evaluating Eq. 1 at the airfoil nodes gives a vector of N streamfunction values,

$$\mathbf{\Psi} = \mathbf{\Psi}^\infty + \mathbf{A}\boldsymbol{\gamma} + \mathbf{B}\boldsymbol{\sigma} \quad \mathbf{A} \in \mathbb{R}^{N \times N}, \ \mathbf{B} \in \mathbb{R}^{N \times (N+N_w-2)}, \tag{3}$$

where $\boldsymbol{\gamma} \in \mathbb{R}^N$ contains the airfoil node vortex strengths and $\boldsymbol{\sigma} \in \mathbb{R}^{N+N_w-2}$ contains both the airfoil and wake panel source strengths. The Kutta condition of smooth flow off the trailing edge provides an additional equation, $\gamma_1 + \gamma_N = 0$. Setting the streamfunction equal to Ψ_0, an additional unknown, at each airfoil node yields a $(N+1) \times (N+1)$ system of equations for $\boldsymbol{\gamma}$ and Ψ_0. Solving this system gives

$$\widetilde{\boldsymbol{\gamma}} = -\widetilde{\mathbf{A}}^{-1} \left(\widetilde{\mathbf{\Psi}}^\infty + \widetilde{\mathbf{B}}\boldsymbol{\sigma} \right) \tag{4}$$

where $\widetilde{\boldsymbol{\gamma}} = [\boldsymbol{\gamma}, \Psi_0]^T$, $\widetilde{\mathbf{A}}$ is $\mathbf{A}$ augmented with the Kutta condition and effects of Ψ_0, and $\widetilde{\mathbf{B}}$ is $\mathbf{B}$ padded with an extra row of zeros. Without viscous sources, Eq. (4) constitutes the inviscid solution, which can be separated into 0 and 90° reference solutions as $\widetilde{\boldsymbol{\gamma}}^i = -\widetilde{\mathbf{A}}^{-1}\widetilde{\mathbf{\Psi}}^\infty = \widetilde{\boldsymbol{\gamma}}_0 \cos \alpha + \widetilde{\boldsymbol{\gamma}}_{90} \sin \alpha$. Since the flow inside the airfoil is stagnant, γ equals the tangential velocity at the airfoil surface.

For an airfoil without a trailing-edge gap, nodes 1 and N coincide, so that the Nth row of the system in Eq. (3) duplicates the first. The Nth row is then replaced by an extrapolation of the change in γ between the lower and upper surfaces: $\gamma_N - \gamma_1 = 2(\gamma_2 - \gamma_{N-1}) - (\gamma_3 - \gamma_{N-2})$ [1].

IV. Viscous Formulation

A. Boundary-Layer Equations

The integral boundary layer equations model the viscous flow and affect the inviscid solution through displacement effects. In turn, the inviscid solution affects the boundary layer through the edge velocity. Separate boundary layer solutions exist on the upper and lower surfaces, and in

the wake. Let ξ be the distance from the leading edge stagnation point for one such surface. The governing boundary layer equations on that surface read [1, 13, 22].

$$\frac{1}{\theta}\frac{d\theta}{d\xi} + (2 + H + H^w - M_e^2)\frac{1}{u_e}\frac{du_e}{d\xi} = \frac{c_f}{2\theta} \quad \text{(momentum)} \tag{5}$$

$$\frac{1}{H^*}\frac{dH^*}{d\xi} + \left(2\frac{H^{**}}{H^*} + 1 - H - H^w\right)\frac{1}{u_e}\frac{du_e}{d\xi} = \frac{2c_D}{\theta H^*} - \frac{c_f}{2\theta} \quad \text{(shape parameter)} \tag{6}$$

$$\frac{d\tilde{n}}{d\xi} = \frac{d\tilde{n}}{dRe_\theta}\frac{dRe_\theta}{d\xi} \quad \text{(amplification)} \tag{7}$$

$$\frac{\delta}{c_\tau^{1/2}}\frac{dc_\tau^{1/2}}{d\xi} - \frac{K_{\text{lag}}}{G_\beta(1+U_s)}(c_{\tau,\text{eq}}^{1/2} - \eta_D c_\tau^{1/2}) = 2\delta\left(u_q - \frac{1}{u_e}\frac{du_e}{d\xi}\right) \quad \text{(turbulent shear lag)} \tag{8}$$

The amplification equation pertains to the growth of the amplitude of the most amplified Tollmien-Schlichting wave and applies only in laminar regions. The turbulent shear lag equation models the evolution of the maximum shear stress coefficient, c_τ, to account for deviations of outer layer dissipation from its local equilibrium value. It only applies in the turbulent region, which includes the entire wake.

The boundary layer equations are discretized by finite differences on the airfoil and wake nodes. At each node i, the state vector consists of four quantities, $\mathbf{u}_i = [\theta, \delta^*, \tilde{n} \text{ or } c_\tau^{1/2}, u_e]^T$. To interpret the third state, a separate flag indicates whether a node is laminar or turbulent.

B. Boundary-Layer Residuals

Considering adjacent nodes 1 and 2, the discretized equations read

$$R_{\text{mom}} \equiv \ln\frac{\theta_2}{\theta_1} + (2 + H + H^w - M_e^2)\ln\frac{u_{e2}}{u_{e1}} - \frac{1}{2}\ln\frac{\xi_2}{\xi_1}\frac{c_f\xi}{\theta} \tag{9}$$

$$R_{\text{shape}} \equiv \ln\frac{H_2^*}{H_1^*} + \left(2\frac{H^{**}}{H^*} + 1 - H - H^w\right)\ln\frac{u_{e2}}{u_{e1}} + \ln\frac{\xi_2}{\xi_1}\left(\frac{1}{2}\frac{c_f\xi}{\theta} - \frac{c_D\xi}{\theta H^*}\right) \tag{10}$$

$$R_{\text{amp}} \equiv \eta_2 - \eta_1 - \frac{d\tilde{n}}{d\xi}\Delta\xi \tag{11}$$

$$R_{\text{lag}} \equiv 2\delta\ln\frac{c_{\tau2}^{1/2}}{c_{\tau1}^{1/2}} - \frac{K_{\text{lag}}}{G_\beta(1+U_s)}(c_{\tau,\text{eq}}^{1/2} - \eta_D c_\tau^{1/2})\Delta\xi - 2\delta\left(u_q\Delta\xi - \ln\frac{u_{e2}}{u_{e1}}\right) \tag{12}$$

The derivation of these equations uses finite differences of logarithms for terms such as $\frac{1}{\theta}\frac{d\theta}{d\xi} = \frac{d}{d\theta}\ln\theta$. Including ξ with the c_f and c_D terms in the momentum and shape equations, i.e. $\frac{c_f}{\theta} = \frac{1}{\xi}\frac{c_f\xi}{\theta} = \frac{d}{d\xi}(\ln\xi)\frac{c_f\xi}{\theta}$, improves accuracy and stability near stagnation, as c_f and c_D depend inversely on u_e, which depends directly on ξ at stagnation.

The appendix presents closure relations for the quantities that appear in the residuals. In the discretized equations, quantities without a subscript of 1 or 2 are determined by symmetrical

averaging from the nodes, consistent with trapezoidal integration, or upwinding, which improves stability with a bias towards backward Euler. The upwinding factor between nodes 1 and 2, used as e.g. $H = (1 - \eta_{\text{up}})H_1 + \eta_{\text{up}}H_2$, depends on the kinematic shape parameter,

$$\eta_{\text{up}} = 1 - \frac{1}{2} \exp\left(-(\ln|f_{Hu}|)^2 \frac{C_{\text{up}}}{H_{k2}^2}\right), \quad f_{Hu} = \frac{H_{k2} - 1}{H_{k1} - 1} \tag{13}$$

where C_{up} equals 1 on the airfoil and 5 in the wake. The larger value in the wake derives from the original XFOIL implementation and improves stability of the solver. In the momentum equation, all quantities are averaged and the term $\frac{c_f \xi}{\theta}$ is treated together. Further averaging $\frac{c_f \xi}{\theta}$ with an evaluation at the midpoint state improves accuracy of the drag calculation. In the shape parameter equation, the skin friction and dissipation terms, $\frac{c_f \xi}{\theta}$ and $\frac{c_D \xi}{\theta H^*}$, are upwinded, while the other terms are averaged. In the amplification equation, $\frac{d\tilde{n}}{d\xi}$ is averaged. In the shear lag equation, $c_\tau^{1/2}$ and $c_{\tau,\text{eq}}^{1/2}$ are upwinded, δ is averaged, and u_q is computed using an upwinded c_f and H_k, and an averaged δ^* and Re_θ.

C. Stagnation-Point Treatment

The leading-edge stagnation point, defined as the location on the airfoil surface at which $u_e = 0$, separates the upper and lower surfaces of the airfoil. The distance from the leading edge of a point on the airfoil surface or wake is then $\xi \equiv |s - s_{\text{stag}}|$, where s is the spline arclength. The s-value of the stagnation point, s_{stag} is determined by linearly interpolating the edge velocity and s values of the nodes adjacent to the stagnation interval, $s_{\text{stag}} = (u_{e2}s_1 + u_{e1}s_2)/(u_{e1} + u_{e2})$. The sign of the edge velocity is positive away from the stagnation point, and hence a negative u_{e1} or u_{e2} in the course of a calculation indicates that the stagnation interval must move. A direction factor, $d_i \pm 1$, at each airfoil and wake node aids in mapping the clockwise node ordering direction to the local downstream direction: i.e. $d_i = -1$ on the lower surface nodes.

The discretized equations apply between two nodes on a given surface or wake. These equations change for the interval between stagnation and the first node, as only one state is available. The modified equations dictate the value of variables at stagnation and pertain to momentum and shape parameter, as the amplification rate is assumed to be zero on the first interval. At stagnation, $\xi, u_e \to 0$, so the first terms in Eqs. (5) and (6) become negligible relative to the others, which have u_e in the denominator. Thus, $\ln \frac{\theta_2}{\theta_1}$ and $\ln \frac{H_2^*}{H_1^*}$ drop out of the discretized equations. Also, writing $u_e \approx K\xi$ (first term in Taylor series) at stagnation means that $\ln \frac{u_{e2}}{u_{e1}} = \ln \frac{\xi_2}{\xi_1}$, and without loss of generality, both of these terms can be set to 1. The resulting two equations are closed and yield the stagnation values of θ and δ^*. Applying this equation to the first node state makes the assumption that the first node and stagnation point are the same, which can cause inaccuracy and unstable oscillations in the variables. At a cost of slightly higher bandwidth in the residual Jacobian matrix, a

8

more accurate and stable solution follows from applying the stagnation point equations to a state linearly extrapolated from the first two nodes to $\xi = 0$. For further accuracy improvement, the edge velocity slope at stagnation, $K = \frac{du_e}{d\xi}$, is calculated from a quadratic fit of u_e at stagnation and the first two nodes. In the unlikely case that the stagnation point coincides, to machine precision, with a panel node, the stagnation equations apply to that node.

D. Wake Discretization and Initialization

An accurate viscous flow approximation requires solution of the boundary layer variables in the airfoil wake. The inviscid solution defines the wake geometry as the streamline emanating from the midpoint of the trailing edge, as shown in Figure 1. Starting with the first wake point a distance $\epsilon^w c$ downstream of the trailing edge midpoint, a predictor-corrector method produces the subsequent wake nodes, totalling $N^w = [N/10 + 10d^w]$ and spaced geometrically until a total wake length of $d^w c$.

A separate set of three equations defines the first wake node state in terms of the airfoil trailing edge states 1 and N,

$$R_{\text{mom}}^w \equiv \theta_1^w - \theta_1 - \theta_N, \quad R_{\text{shape}}^w \equiv \delta_1^{*w} - \delta_1^* - \delta_N^* - h_{\text{TE}}, \quad R_{\text{lag}}^w \equiv c_{\tau 1}^{1/2\,w} - \frac{\theta_1 c_{\tau 1}^{1/2} + \theta_N c_{\tau N}^{1/2}}{\theta_1 + \theta_N} \quad (14)$$

If the state at node 1 or N is laminar, transition to turbulence is forced and $c_\tau^{1/2}$ is calculated using the transition equation, Eq. (17). The wake displacement thickness includes the trailing edge gap, which starts at $h_1^w = h_{TE}$ for the first wake node and decreases to zero at a distance $L^w = f^w h_{TE}$ away from the trailing edge according to [23]

$$h^w(\xi^w) = h_{TE} \left[1 + \left(2 + f^w \frac{dt}{d\xi} \right) \frac{\xi^w}{L^w} \right] \left(1 - \frac{\xi^w}{L^w} \right)^2 \quad (15)$$

where ξ^w is the distance along the wake from the trailing edge, and $\frac{dt}{d\xi}$ is the TE airfoil thickness slope, clipped to lie between $\pm 3/f^w$. The value h^w is subtracted from the displacement thickness at the affected wake nodes for use in the boundary layer equations. The momentum and shape equations explicitly add h^w back into δ^* to obtain the shape parameter with the true displacement thickness, $H + H^w$, where $H^w = h^w/\theta$.

E. Transition Prediction

To predict transition, the present approach uses the e^9 method [13, 24], as in XFOIL. The amplification factor, $\tilde{n}$, starts at zero at the leading-edge stagnation point and evolves downstream according to Eq. (7). Once $\tilde{n}$ exceeds $\tilde{n}_{\text{crit}}$, the boundary layer transitions to turbulent and the shear

lag equation, Eq. (8) replaces the amplification factor equation. The discrete interval over which transition occurs requires special treatment to predict the transition location.
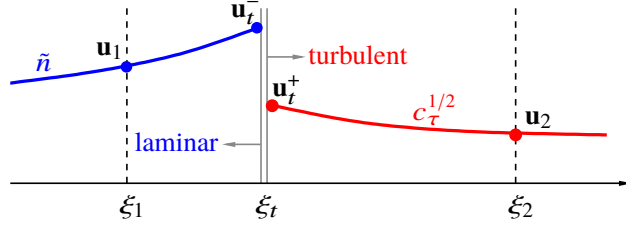

Fig. 4   Transition interval definitions.

Figure 4 illustrates the quantities used in analyzing a transition interval. The switch in equations and variables occurs at the transition location, ξ_t. The discrete boundary layer equations applied separately over the laminar interval, ξ_1 to ξ_t, and the turbulent interval, ξ_t to ξ_2, yield two sets of residuals, which are summed together in the global system,

$$\mathbf{R}_{\text{tran}} \equiv \underbrace{\mathbf{R}(\mathbf{u}_1, \xi_1; \mathbf{u}_t^-, \xi_t)}_{\text{laminar}} + \underbrace{\mathbf{R}(\mathbf{u}_t^+, \xi_t; \mathbf{u}_2, \xi_2)}_{\text{turbulent}} \tag{16}$$

where $\mathbf{R} \equiv [R_{\text{mom}}, R_{\text{shape}}, R_{\text{amp}} \text{ or } R_{\text{lag}}]^T$ and the arguments indicate the endpoint states and coordinates for the particular subinterval. The state variables θ, δ^*, and u_e at transition, $\mathbf{u}_t$, are obtained by linearly interpolating the states from nodes 1 and 2 to ξ_t. On the laminar side of transition, $\mathbf{u}_t^-$, the amplification factor is $\tilde{n} = \tilde{n}_{\text{crit}}$, whereas on the turbulent side, $\mathbf{u}_t^+$, the shear stress coefficient is initialized to

$$c_\tau^{1/2} = C_\tau e^{-E_\tau/(H_k-1)} c_{\tau,\text{eq}}^{1/2} \tag{17}$$

The discretized amplification equation, Eq. (11), on the laminar subinterval implicitly defines the transition location via the residual

$$R_t \equiv R_{\text{amp}}(\mathbf{u}_1, \xi_1; \mathbf{u}_t^-, \xi_t) = 0 \tag{18}$$

For given endpoint states $\mathbf{u}_1, \mathbf{u}_2$, a Newton-Raphson solver yields ξ_t and its derivatives with respect to the state variables and node coordinates for addition to the global system. The requirement that the transition residual remain zero constrains the derivatives. For example, the calculation of the derivative of ξ_t with respect to the state at node 1 proceeds as follows:

$$0 = \delta R_t = \frac{\partial R_t}{\partial \mathbf{u}_1} \delta \mathbf{u}_1 + \frac{\partial R_t}{\partial \xi_t} \delta \xi_t \quad \Rightarrow \quad \frac{\partial \xi_t}{\partial \mathbf{u}_1} = -\left(\frac{\partial R_t}{\partial \xi_t}\right)^{-1} \frac{\partial R_t}{\partial \mathbf{u}_1} \tag{19}$$

10

A similar calculation yields derivatives with respect to $\mathbf{u}_2, \xi_1$, and ξ_2. These derivatives then appear in the linearization of the transition residual, Eq. (16), for the global system.

On the way to the converged solution, the location of transition can move within a panel or across panels, with the latter more likely in the initial solver iterations. Following each state update in the solver, the transition location is recalculated on both airfoil surfaces by marching the amplification equation from the stagnation point, using the updated state. This marching further updates the amplification factor at the laminar nodes* and stops upon reaching the transition interval, identified when $\tilde{n}$ exceeds $\tilde{n}_{\text{crit}}$. If the new interval is upstream of the previous one, the previously laminar nodes between the two intervals are initialized to turbulent, with $c_{\tau}^{1/2}$ linearly interpolated from the transition value, Eq. (17), to the first turbulent node after the original transition interval. If the transition interval moves downstream, the amplification factor on the newly identified laminar nodes is already set from marching, and no further re-initialization is required. Similarly, no action is required if the transition interval remains the same, as the transition residual calculation accounts for movements of ξ_t within an interval.

V. Coupled Solver

A. Initialization

The coupled inviscid-viscous Newton solver requires an initial guess for the boundary layer variables. A segregated solution provides this guess: solving the inviscid problem first, without viscous sources, yields the wake shape and a baseline edge velocity u_e at each node. A marching procedure on each airfoil surface follows, starting at the first point after the leading edge, which is set to the stagnation state. On each subsequent interval, the residuals from Eqs. (9)-(12) provide three implicit equations for the three unknown states, $\theta, \delta^*, \tilde{n}$ or $c_{\tau}^{1/2}$, at the next node. This "direct" marching mode can fail, however, particularly close to separation [25]. When the Newton-Raphson solver fails to converge, or when the kinematic shape parameter exceeds $H_{k,\text{max}}$, 3.8 for laminar and 2.5 for turbulent flow, an "inverse" mode is attempted. In the inverse mode, u_e returns as a state variable, and a prescribed H_k change provides the fourth equation that closes the system. Between nodes 1 and 2, this change is

$$
\begin{align}
H_{k2} &= \max(H_{k1} + .03\Delta H_k, H_{k\,\text{max,lam}}) \quad \text{(laminar)} \tag{20}\\
H_{k2} &= \max(H_{k1} - .15\Delta H_k, H_{k\,\text{max,turb}}) \quad \text{(turbulent)} \tag{21}\\
H_{k2} &= H_{k2} - \frac{H_{k2} + .03\Delta H_k(H_{k2} - 1)^3 - H_k}{1 + .09\Delta H_k(H_{k2} - 1)^2} \quad \text{(wake)} \tag{22}
\end{align}
$$

---

*The amplification factor does not directly affect the other residuals, so updating it again in an additional segregated step does not destroy the quadratic convergence of the Newton-Raphson solver.

where $\Delta H_k \equiv (\xi_2 - \xi_1)/\theta_1$. The wake definition is implicit and six iterations are performed starting from $H_{k2} = H_{k1}$. The inverse mode can also fail, although much less frequently than the direct mode. In the event of failure, the state at node 2 is constructed by scaling θ and δ^* from node 1 by $(\xi_2/\xi_1)^{.5}$ (on the airfoil), and by using the inviscid edge velocity. In the wake, the extrapolation is $\theta_2 = \theta_1$ and $\delta_2^* = (\delta_1^* + \theta_1 r)/(1 + r)$, where $r = (\xi_2 - \xi_1)/(10\delta_1^*)$. While heuristic, these equations generally provide adequate initialization for the Newton-Raphson solver.

During initialization of the boundary layer on the airfoil, if the updated amplification factor, $\tilde{n}_2$, exceeds $\tilde{n}_{\mathrm{crit}}$, that interval is solved again using the transition residual, Eq. 16, in place of the original residual. The subsequent nodes are then marked as turbulent. If the flow remains laminar at the airfoil trailing edge, transition is forced at the start of the wake, and the wake residuals, Eqs. 14, define the first wake state.

B. Coupling with the Inviscid Solution

The boundary layer displacement thickness affects the potential flow solution through a transpiration boundary condition [22], modeled by source sheets on the wake and airfoil panels, as shown in Figure 1. Defining the missing "mass" flow, density excluded, as $m \equiv u_e \delta^*$, the local source sheet strength is $\sigma = \frac{dm}{d\xi}$ [1]. The discretized version of this equation on the panel between nodes i and $i + 1$ reads

$$\sigma_i = \frac{m_{i+1} d_{i+1} - m_i d_i}{s_{i+1} - s_i} \quad \Rightarrow \quad \boldsymbol{\sigma} = \mathbf{D}'\mathbf{m} \tag{23}$$

where $\boldsymbol{\sigma}$ consists of sources on both the airfoil and wake panels, and $\mathbf{D}' \in \mathbb{R}^{(N+N^w-2)\times(N+N^w)}$ maps the mass flow vector at the nodes, $\mathbf{m}$, to $\boldsymbol{\sigma}$. Eq. 23 remains valid across the stagnation interval, where the sum of the mass flows dictates the source strength, due to the presence of the direction factors d_i and d_{i+1}.

The potential flow solution affects the boundary layer equations through the edge velocity, u_e. On the airfoil nodes, γ_i equals the clockwise tangential velocity, so $u_{e_i} = d_i \gamma_i$. On the wake nodes, the velocity is calculated by summing contributions from the freestream and all vortex and source sheets,

$$\mathbf{u}_e^w = \mathbf{u}_e^{w,\infty} + \mathbf{C}^\gamma \boldsymbol{\gamma} + \mathbf{C}^\sigma \boldsymbol{\sigma} \tag{24}$$

where $u_{e,i}^{w,\infty} = V_\infty(\cos\alpha \hat{i} + \sin\alpha \hat{k}) \cdot \hat{t}_i^w$ is the freestream contribution, $\hat{t}_i^w$ is the unit tangent vector along the wake at node i, $\mathbf{C}^\gamma \in \mathbb{R}^{N^w \times N}$ accounts for the effect of the airfoil vortex sheet strengths, and $\mathbf{C}^\sigma \in \mathbb{R}^{N^w \times (N+N^w-2)}$ accounts for the effect of the airfoil and wake source strengths.

From Eq. (4), the vector of vortex strengths on the airfoil nodes can be written as $\boldsymbol{\gamma} =$

$\gamma_0 \cos \alpha + \gamma_{90} \sin \alpha + \mathbf{B}'\boldsymbol{\sigma}$, where $\mathbf{B}' \in \mathbb{R}^{N \times (N+N^w-1)}$. Substituting this expression into the expressions for the edge velocity on the airfoil and wake gives

$$
\begin{aligned}
\text{airfoil:} \quad \mathbf{u}_e^a &= \text{diag}(\mathbf{d}^a) \left[\gamma_0 \cos \alpha + \gamma_{90} \sin \alpha + \mathbf{B}'\boldsymbol{\sigma} \right] & = \mathbf{u}_e^{a,\text{inv}} + \mathbf{D}^a \mathbf{m} \\
\text{wake:} \quad \mathbf{u}_e^w &= \mathbf{u}_e^{w,\infty} + \mathbf{C}^\gamma \left[\gamma_0 \cos \alpha + \gamma_{90} \sin \alpha + \mathbf{B}'\boldsymbol{\sigma} \right] + \mathbf{C}^\sigma \boldsymbol{\sigma} & = \mathbf{u}_e^{w,\text{inv}} + \mathbf{D}^w \mathbf{m}
\end{aligned}
\tag{25}
$$

where in the second steps, Eq. (23) replaced $\boldsymbol{\sigma}$ in terms of $\mathbf{m}$, resulting in the matrices $\mathbf{D}^a = \text{diag}(\mathbf{d})\mathbf{B}'\mathbf{D}' \in \mathbb{R}^{N \times (N+N^w)}$ and $\mathbf{D}^w = (\mathbf{C}^\gamma \mathbf{B}' + \mathbf{C}^\sigma)\boldsymbol{\sigma} \in \mathbb{R}^{N^w \times (N+N^w)}$. The vector $\mathbf{d}^a$ contains the N direction factors d_i on the airfoil.

Combining these expressions yields the potential flow edge velocity on all nodes, airfoil and wake,

$$
\mathbf{u}_e = \mathbf{u}_e^{\text{inv}} + \mathbf{D}\mathbf{m}
\tag{26}
$$

where $\mathbf{D} = [\mathbf{D}^a; \mathbf{D}^w] \in \mathbb{R}^{(N+N^w) \times (N+N^w)}$ depends only on the airfoil and wake geometry, and the inviscid solution is stored as two reference vectors, so that $\mathbf{u}_e^{\text{inv}} = \mathbf{u}_{e,0}^{\text{inv}} \cos \alpha + \mathbf{u}_{e,90}^{\text{inv}} \sin \alpha$. In a converged coupled solution, this potential-flow expression for the edge velocity must match the edge velocity stored in the boundary-layer state vector. Enforcing this equality at each airfoil and wake node yields the residual vector

$$
\mathbf{R}_u \equiv \mathbf{u}_e - \left[\mathbf{u}_e^{\text{inv}} + \mathbf{D}(\mathbf{u}_e . \boldsymbol{\delta}^*) \right]
\tag{27}
$$

where in the mass flow expression, the product between $\mathbf{u}_e$ and $\boldsymbol{\delta}^*$ is element-wise. This is the fourth set of equations that closes the global system.

C. Global System Solution

The global system contains $4N^{\text{tot}}$ unknowns, where $N^{\text{tot}} = N + N^w$, consisting of state vectors on every airfoil and wake node. Marching through the panels on the three surfaces (lower, upper, wake) yields three residuals per panel, Eqs. (9)-(12). The stagnation point system and the wake initialization provide the starting-node residuals on the airfoil and wake surfaces. Finally, Eq. (27) provides the additional fourth residual for each node.

Most of the sparse residual Jacobian matrix is populated concurrently with the residual calculation at each panel. To account for movement of the stagnation point, derivatives of the three panel residuals with respect to ξ, which is measured from the stagnation point coordinate s_{stag}, are also calculated and stored in the sparse matrix $\frac{\partial \mathbf{R}'}{\partial \boldsymbol{\xi}} \in \mathbb{R}^{(3N^{\text{tot}}) \times N^{\text{tot}}}$, where $\mathbf{R}' \in \mathbb{R}^{3N^{\text{tot}}}$ contains the panel residuals, and $\boldsymbol{\xi} \in \mathbb{R}^{N^{\text{tot}}}$ stores the surface ξ coordinate of each node. As the stagnation point location depends on the edge velocity, the required addition to the residual Jacobian matrix occurs in the $\mathbf{u}_e$

columns,

$$\frac{\partial \mathbf{R}'}{\partial \mathbf{u}_e} \mathrel{+}= \frac{\partial \mathbf{R}'}{\partial \boldsymbol{\xi}} \frac{\partial \boldsymbol{\xi}}{\partial s_{\text{stag}}} \frac{\partial s_{\text{stag}}}{\partial \mathbf{u}_e} \tag{28}$$

where $\frac{\partial \boldsymbol{\xi}}{\partial s_{\text{stag}}} = -\mathbf{d}$ is the opposite of the nodal direction vector, and $\frac{\partial s_{\text{stag}}}{\partial \mathbf{u}_e} \in \mathbb{R}^{1 \times (N+N^w)}$ contains only two nonzero entries corresponding to the edge velocities adjacent to the stagnation interval. Hence, the step in Eq. 28 increments only two columns of the residual Jacobian matrix.

In a lift-constrained run with a target lift coefficient $c_{\ell,\text{tgt}}$, an extra residual, $R^{c_\ell} \equiv c_\ell(\mathbf{u}) - c_{\ell,\text{tgt}}$, augments the global system to allow solution for the unknown angle of attack, α. Derivatives of R^{c_ℓ} with respect to the state and angle of attack are computed during the c_ℓ calculation. In the additional column of the Jacobian matrix, $\frac{\partial \mathbf{R}'}{\partial \alpha} = \mathbf{0}$ for the three boundary-layer residuals, and, by Eq. 27, $\frac{\partial \mathbf{R}^u}{\partial \alpha} = -\frac{\partial \mathbf{u}_e^{\text{inv}}}{\partial \alpha} = \mathbf{u}_{e,0}^{\text{inv}} \sin \alpha - \mathbf{u}_{e,90}^{\text{inv}} \cos \alpha$.

At each Newton iteration, a sparse linear solver yields the state update, $\Delta \mathbf{u} \in \mathbb{R}^{N^{\text{tot}}}$, and the angle of attack update $\Delta \alpha$ in lift-constrained mode. Limiting this update with an under-relaxation factor, ω, prevents non-physical states and divergence of the solver. A single global value of ω is calculated such that: θ and δ^* do not decrease by more than 50%; $\tilde{n}$ and $c_\tau^{1/2}$ values greater than 0.2 and $0.1 \max(c_\tau^{1/2})$, respectively, do not decrease by more than 80% (very small values are not limited); $\tilde{n}$ does not increase by more than 2; $c_\tau^{1/2}$ does not increase by more than .05; u_e does not change by more than 20%; α does not change by more than 2°. In addition, after the update, negative $c_\tau^{1/2}$ values are clipped to $0.1 \max(c_\tau^{1/2})$, and the value of δ^* on each node is increased to ensure that $H_k > H_{k,\text{min}}$, where $H_{k,\text{min}} = 1.00005$ on the airfoil and 1.02 in the wake. Changes in the angle of attack require rebuilding the inviscid solution and potentially the wake, although an option exists to keep the wake fixed at the inviscid-trimmed angle of attack.

VI. Compressibility Correction

The potential flow solution presented thus far applies to incompressible flow. A compressibility correction extends its applicability to subcritical compressible flow. As in XFOIL, the present work uses the Kármán-Tsien compressibility correction [26], which consists of nonlinear corrections to the incompressible speed, V_{inc}, and pressure coefficient, $c_{p,\text{inc}}$,

$$V = \frac{V_{\text{inc}}(1 - \lambda)}{1 - \lambda(V_{\text{inc}}/V_\infty)^2}, \quad c_p = \frac{c_{p,\text{inc}}}{\beta + \lambda(1 + \beta)c_{p,\text{inc}}/2}, \quad \lambda = \frac{M_\infty^2}{(1 + \beta)^2}, \quad \beta = \sqrt{1 - M_\infty^2} \tag{29}$$

Although the boundary-layer equations apply as written in compressible flow, notably through the inclusion of the edge Mach number, M_e, in Eq. 5, the velocity correction has several widespread, albeit subtle, effects. First, the edge velocity computed from the potential flow solution and stored

as a boundary layer state corresponds to the incompressible edge velocity, $u_{e,\text{inc}}$. Applying the correction yields the compressible edge velocity, u_e, as a function of $u_{e,\text{inc}}$ and M_∞. The edge Mach number calculation, $M_e = u_e/c_{\text{air}}$ requires the *local* speed of sound, c_{air}, which depends on the temperature and hence the corrected speed through

$$c_{\text{air}}^2 = (\gamma_{\text{air}} - 1)\left(H_0 - \frac{u_e^2}{2}\right), \quad H_0 = \frac{V_\infty^2}{(\gamma_{\text{air}} - 1)M_\infty^2}\left(1 + \frac{\gamma_{\text{air}} - 1}{2}M_\infty^2\right) \tag{30}$$

where H_0 is the constant stagnation enthalpy. The momentum-thickness Reynolds number calculation $Re_\theta = \rho u_e \theta/\mu$ also requires the local density, ρ, and dynamic viscosity, μ. Isentropic relations yield the density,

$$\rho = \rho_0\left(1 + \frac{\gamma_{\text{air}} - 1}{2}M_e^2\right)^{-1/(\gamma_{\text{air}}-1)}, \quad \rho_0 = \rho_\infty\left(1 + \frac{\gamma_{\text{air}} - 1}{2}M_\infty^2\right)^{1/(\gamma_{\text{air}}-1)} \tag{31}$$

and Sutherland's law yields the dynamic viscosity,

$$\mu = \mu_0\text{Su}\left(\frac{T}{T_0}\right), \quad \mu_0 = \mu_\infty\text{Su}\left(\frac{T_\infty}{T_0}\right), \quad \text{Su}\left(\frac{T}{T_0}\right) = \left(\frac{T}{T_0}\right)^{1.5}\frac{1 + r_{\text{Su}}}{\frac{T}{T_0} + r_{\text{Su}}}, \quad \frac{T}{T_0} = 1 - \frac{1}{2}\frac{V_\infty^2}{H_0} \tag{32}$$

VII. Post-Processing

Outputs of interest include coefficients of lift, moment, and drag, separated into skin-friction and pressure components. A summation over the airfoil panels, including the trailing-edge gap, yields the lift, moment, and near-field pressure drag coefficients,

$$c_\ell = \frac{1}{c}\int_{\text{airfoil}} c_p\hat{n}\cdot\hat{L}\,ds \approx \frac{1}{c}\sum_{i=1}^N \bar{c}_{p,i}(-\sin\alpha\Delta z_i - \cos\alpha\Delta x_i) \tag{33}$$

$$c_{d,\text{inv}} = \frac{1}{c}\int_{\text{airfoil}} c_p\hat{n}\cdot\hat{D}\,ds \approx \frac{1}{c}\sum_{i=1}^N \bar{c}_{p,i}(\cos\alpha\Delta z_i - \sin\alpha\Delta x_i) \tag{34}$$

$$c_m = \frac{1}{c^2}\int_{\text{airfoil}} c_p[(\vec{x} - \vec{x}_0)\times\hat{n}]\cdot\hat{j}\,ds \approx \frac{1}{c^2}\sum_{i=1}^N [c_{p,i}, c_{p,i+1}]\mathbf{M}\begin{bmatrix}\Delta\vec{x}_i\cdot(\vec{x}_i - \vec{x}_0) \\ \Delta\vec{x}_i\cdot(\vec{x}_{i+1} - \vec{x}_0)\end{bmatrix} \tag{35}$$

where $\hat{L} = -\sin\alpha\hat{i} + \cos\alpha\hat{k}$, $\hat{D} = \cos\alpha\hat{i} + \sin\alpha\hat{k}$, $\bar{c}_{p,i} = (c_{pi} + c_{p,i+1})/2$, $\Delta\vec{x}_i = \vec{x}_{i+1} - \vec{x}_i = \Delta x_i\hat{i} + \Delta z_i\hat{k}$, $\vec{x}_0$ is the moment reference location, and $\mathbf{M} = [2, 1; 1, 2]/6$. The approximation that the pressure coefficient varies linearly across a panel underlies these integrals.

In viscous simulations, the Squire-Young relation [27] provides an accurate approximation of the total drag coefficient by extrapolating the final wake momentum thickness, $c_d = 2\theta\,(u_e/V_\infty)^{(5+H)/2}$.

The quantities θ, u_e, and H in this expression are taken from the final wake node. An integration of the skin friction coefficient over the airfoil lower and upper surfaces yields the skin friction drag coefficient,

$$c_{df} = \frac{D_{f1} + D_{f2}}{\frac{1}{2}\rho_\infty V_\infty^2 c}, \quad D_{fj} = \int_{\text{surface } j} \tau_w \, d\vec{\xi} \cdot \hat{D} \approx \sum_{i=1}^{N_j} \frac{1}{2}(\tau_{w,i-1} + \tau_{w,i})\Delta\vec{x}_j \cdot \hat{D}, \quad \tau_w = \frac{1}{2}\rho c_f u_e^2 \quad (36)$$

where N_j is the number of nodes on surface j, and node 0 corresponds to the stagnation point, where $u_e = 0$. The difference of the total and skin friction drag coefficients yields the pressure drag coefficient, $c_{dp} = c_d - c_{df}$.

VIII. Results

Unless otherwise noted, the following set of results is based on a NACA 2412 airfoil at chord Reynolds number $Re = 10^6$, angle of attack $\alpha = 2°$, and free-stream Mach number $M_\infty = 0.4$. The default number of airfoil points is $N = 200$.

A. Outputs and Distributions

Table 1 presents the outputs computed from the present code, mfoil, in comparison to those obtained from XFOIL. Differences in panel distributions and models cause slight differences in the results, but the overall agreement is very good. Likewise, the distribution quantities in Figure 5 exhibit excellent agreement.

Table 1   NACA 2412, $Re = 10^6$, $\alpha = 2°$, $M_\infty = 0.4$: output comparisons to XFOIL

output	mfoil	XFOIL
lift coefficient	0.4889	0.4910
quarter-chord moment coefficient	-0.0501	-0.0506
drag coefficient	0.00617	0.00618
skin friction drag coefficient	0.00421	0.00421
upper surface transition	$0.4908c$	$0.4901c$
lower surface transition	$0.9487c$	$0.9486c$

The present modifications in the stagnation point treatment, described in Section IV.C, cause noticeable differences in the solution behavior near the stagnation point. Figure 6 shows the kinematic shape factor, which for most of the airfoil and the wake matches that of XFOIL very well. However, a zoom-in at the leading edge shows oscillations in the XFOIL results. These oscillations are due to an inconsistency in the equation for the first boundary layer point on each surface, which
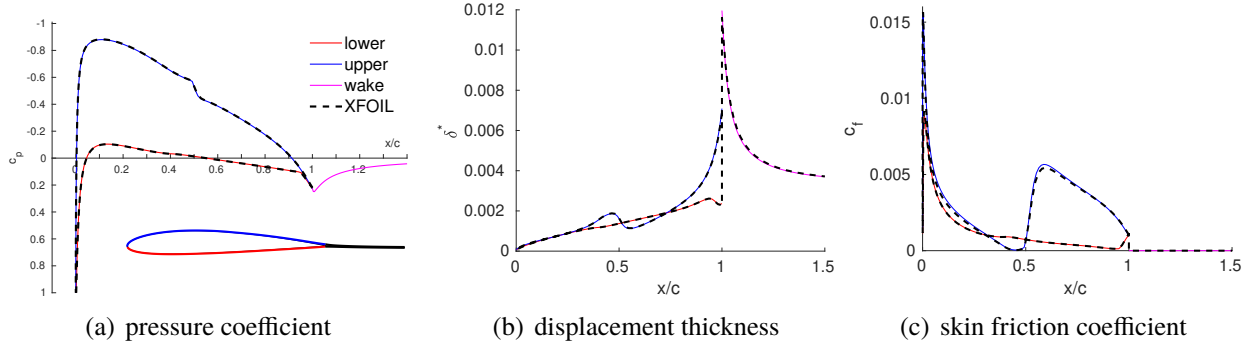
(a) pressure coefficient (b) displacement thickness (c) skin friction coefficient

Fig. 5   NACA 2412, $Re = 10^6$, $\alpha = 2°$, $M_\infty = 0.4$: **comparison of distributions.**

in general is not at stagnation. The oscillations diminish but do not disappear with increasing N. On the other hand, mfoil, with its stagnation point extrapolation and higher-order edge velocity derivative calculation, exhibits a smoother H_k profile. Early-stage convergence of mfoil was found to be less robust without this stagnation point treatment.
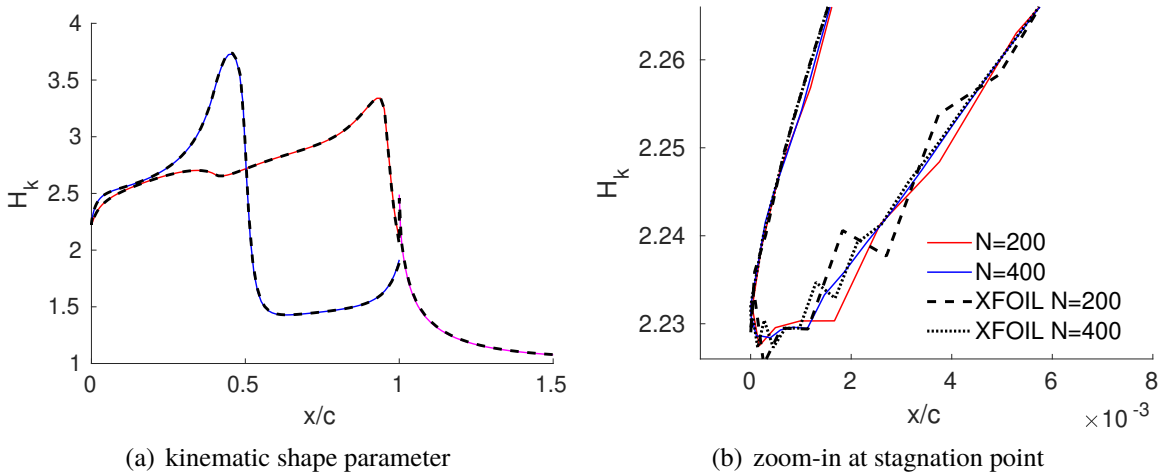

(a) kinematic shape parameter (b) zoom-in at stagnation point

Fig. 6   NACA 2412, $Re = 10^6$, $\alpha = 2°$, $M_\infty = 0.4$: **kinematic shape factor comparison.**

B. Solver Convergence

Following the boundary layer initialization process described in Section V.A, the coupled solver advances the state towards convergence. Since the initialized state may not be close to the converged one, the first Newton iterations proceed slowly, as illustrated in Figure 7(a). Update limiting plays a critical role in keeping the solution physical and preventing divergence in this stage. A sharp residual drop follows the initial residual plateau, characteristic of quadratic Newton-Raphson convergence. The length of the plateau depends on the operating conditions and the number of points: increasing N leads to more iterations. Figure 7(b) shows the lift coefficient output history for both runs.

17

Accurate c_ℓ values do not occur until close to residual convergence.

(a) residual norm

(b) lift coefficient

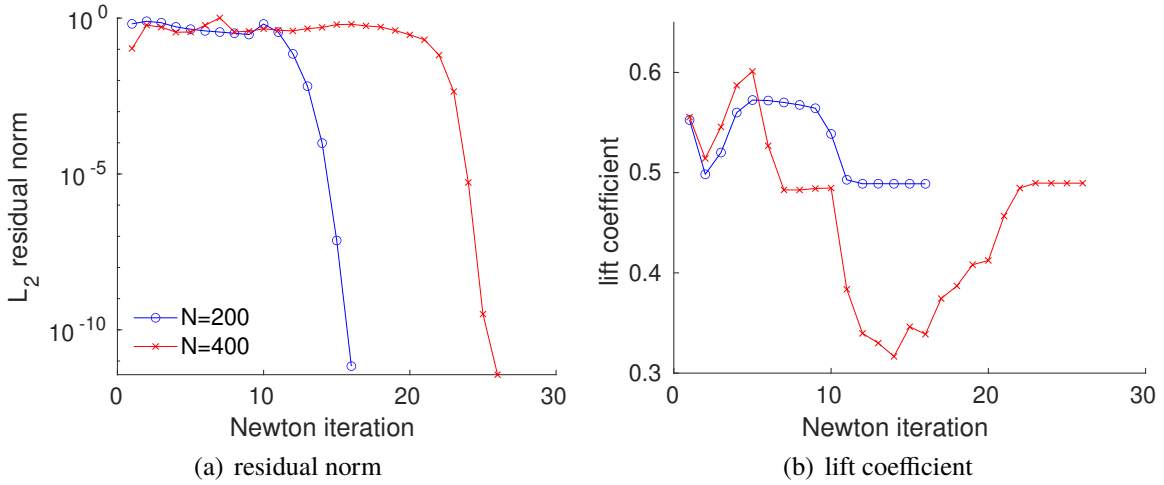**Fig. 7   NACA 2412, $Re = 10^6$, $\alpha = 2°$, $M_\infty = 0.4$: residual and output convergence.**

The amplification factor rate of increase equation contains an extra term, Eq. 76, that ensures that the rate does not stagnate as $\tilde{n} \rightarrow \tilde{n}_{\text{crit}}$. This term differs from a similar one in XFOIL, in its smoother form and positive values after $\tilde{n}_{\text{crit}}$. Without this term, the amplification factor may not cross the critical value when expected, particularly at high Reynolds numbers and on coarse panelings. Figure 8 shows this lack of convergence for the NACA 2412 airfoil at $\alpha = 2°$, $M = 0.4$, $Re = 10^7$. Including the extra term in $\frac{d\tilde{n}}{d\xi}$ yields rapid convergence instead.
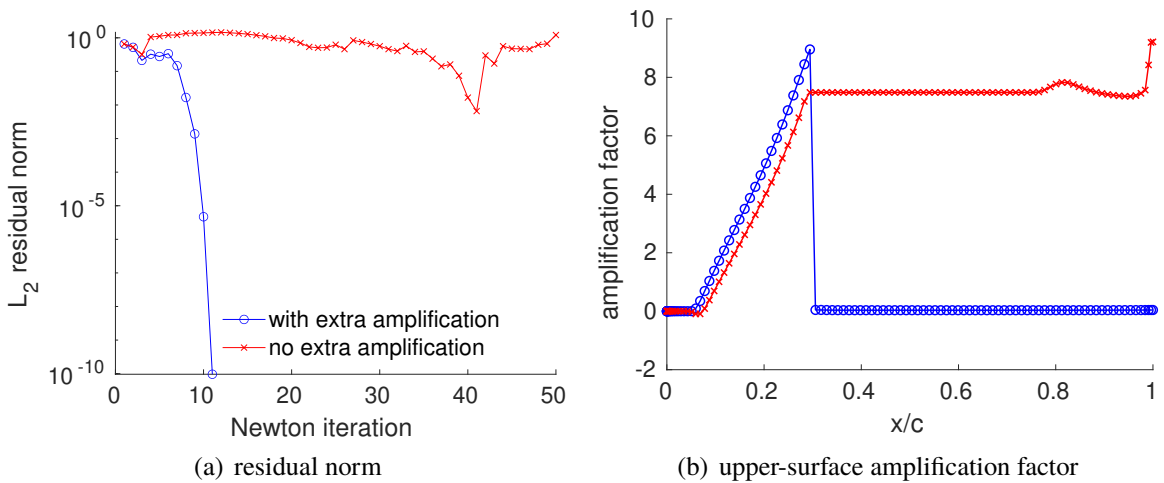

(a) residual norm

(b) upper-surface amplification factor

Fig. 8   NACA 2412, $Re = 10^7$, $\alpha = 2°$, $M_\infty = 0.4$: lack of convergence without extra amplification rate.

C. Geometry Manipulation and Newton Continuation

The code supports airfoil geometry import and manipulation, including camber modification and flap deployment. Built-in splining functions redistribute panel nodes based on surface curvature. High angle of attack simulations with flaps can cause convergence problems due to the near separated nature of the flowfield. Figure 9 illustrates this problem for an $\alpha = 5°$, $Re = 10^6$, $M = 0.2$ simulation of a NACA 2412 airfoil with a $10°$ flap at 80% chord. A direct solution attempt fails due to separation on the upper surface flap hinge, as shown in Figure 9(a). The residual stagnates at a large value and severe update limiting due to a near non-physical state prevents solution advancement. An angle-of-attack continuation strategy aids in such a case: a solution at $\alpha = 0°$ initializes the boundary-layer solution at $\alpha = 2.5°$, which in turn initializes the solution at $\alpha = 5°$, shown in Figure 9(c). Figure 9(b) shows the combined residual history: after the first angle of attack, subsequent solutions proceed more quickly due to a good starting guess. This process can be automated inside or outside the code, using different starting angles of attack and fixed or adaptive increments.
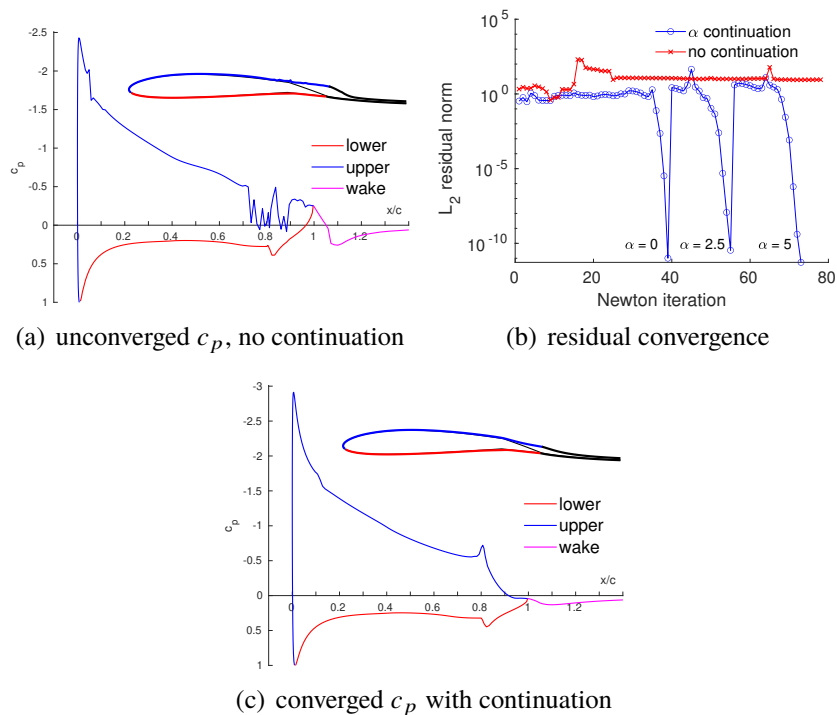

(a) unconverged c_p, no continuation

(b) residual convergence

(c) converged c_p with continuation

Fig. 9   NACA 2412, $Re = 10^6$, $\alpha = 5°$, $M_\infty = 0.2$, $10°$ flap : angle-of-attack continuation.

IX. Conclusion

The speed, robustness, and ease-of-use of the XFOIL airfoil analysis and design code have made it the program of choice for many research studies and educational purposes. Its longevity of

over thirty years and counting is a testament to its methods, implementation, and maintenance. As software and hardware have advanced, however, XFOIL is feeling its age with regard to accessibility and understanding beyond a black-box level. In this work, the XFOIL code has been re-implemented, with certain modifications, in a modular, documented Matlab class, with the purpose of (1) distilling and documenting the models and methods; and (2) providing an accessible implementation in a newer software framework. This paper presents a self-contained and comprehensive exposition of the methods used, as an accompaniment to the code. The results section serves to show agreement with XFOIL, which has undergone multiple previous validations, and performance and robustness enhancements due to several modifications.

Appendix

A. Panel Influence Coefficients

This appendix presents the influence coefficients of linear/constant vortex/source panels that appear in Eqs. (1) and (2). Figure 10 defines the quantities used in calculating the streamfunction and velocity at an arbitrary evaluation point.
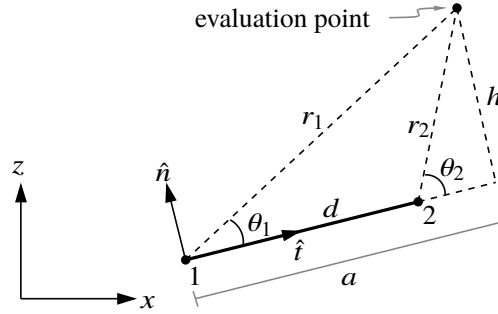

Fig. 10   Geometry definition for a panel of length d.

Vortex panel: Given vortex strengths γ_1 and γ_2 at the two nodes, the streamfunction at the evaluation point is $\Psi = \mathbf{\Psi}^\gamma [\gamma_1, \gamma_2]^T$, where $\mathbf{\Psi}^\gamma = [\bar{\Psi}^\gamma - \widetilde{\Psi}^\gamma, \widetilde{\Psi}^\gamma]$, and

$$\bar{\Psi}^\gamma = \frac{1}{2\pi} \left(h(\theta_2 - \theta_1) - d + a \ln r_1 - (a - d) \ln r_2 \right), \tag{37}$$

$$\widetilde{\Psi}^\gamma = \frac{a}{d} \bar{\Psi}^\gamma + \frac{1}{4\pi d} \left(r_2^2 \ln r_2 - r_1^2 \ln r_1 - \frac{1}{2} r_2^2 + \frac{1}{2} r_2^2 \right) \tag{38}$$

When the evaluation point lies on a panel endpoint, setting the corresponding $\ln r_1$ or $\ln r_2$ to zero avoids a mathematical exception (the streamfunction remains well-defined due to multiplicative factors on these terms that go to zero). The velocity at the evaluation point is $\vec{v} = v_t \hat{t} + v_n \hat{n}$, where

$v_t = (\bar{v}_t - \widetilde{v}_t)\gamma_1 + \widetilde{v}_t\gamma_2$, $v_n = (\bar{v}_n - \widetilde{v}_n)\gamma_1 + \widetilde{v}_n\gamma_2$, and

$$\bar{v}_t = \frac{1}{2\pi}(\theta_2 - \theta_1), \qquad\qquad \widetilde{v}_t = \frac{1}{2\pi d}\left(h \ln \frac{r_2}{r_1} + a(\theta_2 - \theta_1)\right), \qquad (39)$$

$$\bar{v}_n = \frac{1}{2\pi}\ln\frac{r_2}{r_1}, \qquad\qquad \widetilde{v}_n = \frac{1}{2\pi d}\left(a \ln \frac{r_2}{r_1} + d - h(\theta_2 - \theta_1)\right) \qquad (40)$$

Setting $\gamma_1 = \gamma_2 = \gamma$ gives the constant vortex panel result, $\Psi = \Psi^\gamma\gamma$, where $\Psi^\gamma = \bar{\Psi}^\gamma$, and $\vec{v} = (\bar{v}_t\hat{t} + \bar{v}_n\hat{n})\gamma$.

Source panel: Given source strengths σ_1 and σ_2 at the two nodes, the streamfunction at the evaluation point is $\Psi = \mathbf{\Psi}^\sigma[\sigma_1, \sigma_2]^T$, where $\mathbf{\Psi}^\sigma = [\bar{\Psi}^\sigma - \widetilde{\Psi}^\sigma, \widetilde{\Psi}^\sigma]$, and

$$\bar{\Psi}^\sigma = \frac{1}{2\pi}\left(a(\theta_1 - \theta_2) + d\theta_2 + h \ln r_1 - h \ln r_2\right), \qquad (41)$$

$$\widetilde{\Psi}^\sigma = \frac{a}{d}\bar{\Psi}^\sigma + \frac{1}{4\pi d}\left(r_2^2\theta_2 - r_1^2\theta_1 - hd\right) \qquad (42)$$

The streamfunction is singular at the panel endpoints, except in the case of a constant source, $\sigma_1 = \sigma_2 = \sigma$, in which case $\Psi = \Psi^\sigma\sigma = \bar{\Psi}^\sigma\sigma$. Setting the appropriate $\ln r_1$ or $\ln r_2$ to zero avoids a mathematical exception. For a constant source panel, offsetting the streamfunction calculation by $-d/4$ or $3d/4$, depending on the sign of $\theta_1 + \theta_2 - \pi$, positions the branch cut in the $\hat{n}$ direction.

The velocity at the evaluation point is $\vec{v} = v_t\hat{t} + v_n\hat{n}$, where $v_t = (\bar{v}_t - \widetilde{v}_t)\sigma_1 + \widetilde{v}_t\sigma_2$, $v_n = (\bar{v}_n - \widetilde{v}_n)\sigma_1 + \widetilde{v}_n\sigma_2$, and

$$\bar{v}_t = \frac{1}{2\pi}\ln\frac{r_1}{r_2}, \qquad\qquad \widetilde{v}_t = \frac{1}{2\pi d}\left(a \ln \frac{r_1}{r_2} - d + h(\theta_2 - \theta_1)\right), \qquad (43)$$

$$\bar{v}_n = \frac{1}{2\pi}(\theta_2 - \theta_1), \qquad\qquad \widetilde{v}_n = \frac{1}{2\pi d}\left(-h \ln \frac{r_1}{r_2} + a(\theta_2 - \theta_1)\right) \qquad (44)$$

Setting $\sigma_1 = \sigma_2 = \sigma$ gives the constant source panel result $\vec{v} = (\bar{v}_t\hat{t} + \bar{v}_n\hat{n})\sigma$.

B. Closure Equations

This appendix presents the closure relations used in mfoil, which in large part follow those of XFOIL and have previously been documented [1, 13, 23]. Deviations from these references are mainly due to updates to the XFOIL code from the original publications, and present additional modifications, in Eqs. (58), (74), (76), have been made for improved robustness of the Newton-Raphson solver.

The shape parameter closures are

$$H_k = (H - 0.29M_e^2)/(1 + 0.113M_e^2) \tag{45}$$

$$H^{**} = 0.064M_e^2/(H_k - 0.8) \tag{46}$$

$$H_{\text{lam}}^* = \begin{cases} (0.0111\tilde{H}_k^2 - .0278\tilde{H}_k^3)/(H_k - 1) + 1.528 - 0.002(\tilde{H}_k H_k)^2 & \text{if } H_k < 4.35 \\ 0.015\tilde{H}_k^2/H_k + 1.528 & \text{otherwise} \end{cases} \tag{47}$$

$$\tilde{H}_k = H_k - 4.35 \tag{48}$$

$$H_{\text{turb}}^* = (H_{\text{turb,inc}}^* + 0.028M_e^2)/(1 + 0.014M_e^2) \tag{49}$$

$$H_{\text{turb,inc}}^* = \begin{cases} 1.5 + 4/\widetilde{Re}_\theta + 1.5(.5 - 4/\widetilde{Re}_\theta)H_r^2/(H_k + .5) & \text{if } H_k < H_0 \\ 1.5 + 4/\widetilde{Re}_\theta + (H_k - H_0)^2(0.007 \ln \widetilde{Re}_\theta/A_{H^*}^2 + 0.015/H_k) & \text{otherwise} \end{cases} \tag{50}$$

$$H_r = (H_0 - H_k)/(H_0 - 1) \tag{51}$$

$$H_0 = \min(3 + 400/Re_\theta, 4) \tag{52}$$

$$\widetilde{Re}_\theta = \max(Re_\theta, 200) \tag{53}$$

$$A_{H^*} = H_k - H_0 + 4/\ln \widetilde{Re}_\theta \tag{54}$$

$$\delta = \min\left(3.15 + 1.72/(H_k - 1) + \delta^*, 12\theta\right) \tag{55}$$

The skin-friction coefficient is zero in the wake. In laminar and turbulent regions, it is

$$c_{f,\text{lam}} = \frac{1}{Re_\theta} \begin{cases} 0.0727(5.5 - H_k)^3/(H_k + 1) - 0.07 & \text{if } H_k < 5.5 \\ 0.015(1 - 1/(H_k - 4.5))^2 - 0.07 & \text{otherwise} \end{cases} \tag{56}$$

$$c_{f,\text{turb}} = 0.3e^{A_{cf}} B_{cf}^{-1.74 - 0.31H_k} + 0.00011(\tanh(4 - H_k/.875) - 1) \tag{57}$$

$$A_{cf} = -1.33H_k; \text{ if } A_{cf} < -17, A_{cf} = -20 + 3e^{(A_{cf}+17)/3} \tag{58}$$

$$B_{cf} = \max(\log_{10}(Re_\theta/F_c), 1.303) \tag{59}$$

$$F_c = \sqrt{1 + 0.5(\gamma_{\text{air}} - 1)M_e^2} \tag{60}$$

The dissipation coefficient closures are

$$c_{Di,\text{lam}} = \frac{1}{Re_\theta} \begin{cases} 0.00205(4 - H_k)^{5.5} + 0.207 & \text{if } H_k < 4 \\ -0.0016(H_k - 4)^2/(1 + 0.02(H_k - 4)^2) + 0.207 & \text{otherwise} \end{cases} \tag{61}$$

$$c_{Di,\text{turb}} = \min(c_{Di,\text{wall}} + c_{Di,\text{outer}} + c_{Di,\text{stress}},\ c_{Di,\text{lam}}) \tag{62}$$

$$c_{Di,\text{wall}} = \frac{1}{2} c_f U_s (2/H^*) 0.5 \left[1 + \tanh((H_k - 1) \ln(Re_\theta)/2.1) \right] \tag{63}$$

$$c_{Di,\text{outer}} = c_\tau (0.995 - U_s) 2/H^* \tag{64}$$

$$c_{Di,\text{stress}} = 0.3(0.995 - U_s)^2/(H^* Re_\theta) \tag{65}$$

$$c_{Di,\text{wake}} = \min(c_{Di,\text{outer}} + c_{Di,\text{stress}},\ c_{Di,\text{lamwake}}) \tag{66}$$

$$c_{Di,\text{lamwake}} = 2.2(1 - 1/H_k)^2(1/H_k)/(H^* Re_\theta) \tag{67}$$

$$U_s = \frac{1}{2} H^* (1 - (H_k - 1)/(H G_\beta)) \quad (\max 0.98 \text{ on airfoil}, 0.99995 \text{ in wake}) \tag{68}$$

The rate of increase of the amplification factor is

$$\frac{d\tilde{n}}{d\xi} = (r_{\tilde{n}} f_{\tilde{n}} g_{\tilde{n}} + \epsilon_{\tilde{n}})/\theta \tag{69}$$

$$f_{\tilde{n}} = -.05 + 2.7\hat{H} - 5.5\hat{H}^2 + 3\hat{H}^3 + 0.1e^{-20\hat{H}} \tag{70}$$

$$g_{\tilde{n}} = 0.028/\hat{H} - 0.0345 \exp[-(3.87\hat{H} - 2.52)^2] \tag{71}$$

$$r_{\tilde{n}} = \begin{cases} 0 & \text{if } s_{\tilde{n}} < 0 \\ 1 & \text{if } s_{\tilde{n}} > 1 \\ 3s_{\tilde{n}}^2 - 2s_{\tilde{n}}^3 & \text{otherwise} \end{cases} \tag{72}$$

$$s_{\tilde{n}} = (\log_{10} Re_\theta - (L_0 - 0.1))/0.2 \tag{73}$$

$$L_0 = 2.492\hat{H}^{0.43} + 0.7(1 + \tanh(14\hat{H} - 9.24) \tag{74}$$

$$\hat{H} = 1/(H_k - 1) \tag{75}$$

$$\epsilon_{\tilde{n}} = 0.001(1 + \tanh(5(\tilde{n} - \tilde{n}_{\text{crit}})) \tag{76}$$

The equilibrium values of $u_q = \frac{1}{u_e} \frac{du_e}{d\xi}$ and the root shear stress coefficient are

$$u_q = (0.5c_f - (H_{kc}/(G_A \eta_D H_k))^2)/(G_\beta \delta^*) \tag{77}$$

$$H_{kc} = H_k - 1 - \tilde{G}_C/Re_\theta, \quad \tilde{G}_C = 0 \text{ in wake, else } G_C \tag{78}$$

$$c_{\tau,\text{eq}} = H^*(H_k - 1)H_{kc}^2/[(2G_A^2 G_\beta (1 - U_s)HH_k^2] \tag{79}$$

In the above equations, small H_k values are limited to 1.00005 in the wake and 1.05 on the airfoil.

23

C. Parameters

Table 2 lists the default numerical values of the various parameters appearing in the presented equations.

Table 2   Parameter definitions and values

Parameter	Description	Value
γ_{air}	Ratio of specific heats	1.4
η_{crit}	Critical amplification factor	9
G_A	$G - \beta$ locus A constant	6.7
G_B	$G - \beta$ locus B constant	0.75
G_C	$G - \beta$ locus C constant	18.0
η_D	wall/wake dissipation length ratio	0.9 in wake
K_{lag}	shear lag constant	5.6
C_τ	shear stress initialization constant	1.8
E_τ	shear stress initialization exponent	3.3
r_{Su}	Sutherland temperature ratio	0.35
f^w	wake gap continuation factor	2.5
d^w	wake length, in airfoil chords	1
ϵ^w	first wake point offset, in airfoil chords	10^{-5}

References

[1] Drela, M., "XFOIL: An analysis and design system for low Reynolds number airfoils," *Low Reynolds Number Aerodynamics, Lecture Notes in Engineering*, Vol. 54, edited by T. Mueller, Springer Berlin Heidelberg, 1989, pp. 1–12. https://doi.org/10.1007/978-3-642-84010-4_1.

[2] Ronsten, G., "Static pressure measurements on a rotating and a non-rotating 2.375m wind turbine blade. Comparison with 2D calculations," *Journal of Wind Engineering and Industrial Aerodynamics*, Vol. 39, No. 1, 1992, pp. 105–118. https://doi.org/10.1016/0167-6105(92)90537-K.

[3] Giguère, P., and Selig, M., "New Airfoils for Small Horizontal Axis Wind Turbines," *Transactions of the ASME*, Vol. 120, 1998. https://doi.org/10.1115/1.2888052.

[4] Timmer, W. A., and van Rooij, R. P. J. O. M., "Summary of the Delft University Wind Turbine Dedicated Airfoils," *Journal of Solar Energy Engineering*, Vol. 125, No. 4, 2003, pp. 488–496. https://doi.org/10.1115/1.1626129.

[5]   Mueller, T. J., and DeLaurier, J. D., "Aerodynamics of Small Vehicles," *Annual Review of Fluid Mechanics*, Vol. 35, 2003, pp. 89–111. https://doi.org/10.1146/annurev.fluid.35.101101.161102.

[6]   Lafountain, C., Cohen, K., and Abdallah, S., "Use of XFOIL in design of camber-controlled morphing UAVs," *Computer Applications in Engineering Education*, Vol. 20, No. 4, 2012, pp. 673–680. https://doi.org/10.1002/cae.20437.

[7]   Batten, W., Bahaj, A., Molland, A., and Chaplin., J., "Hydrodynamics of Marine Current Turbines," *Renewable Energy*, Vol. 31, No. 2, 2006, pp. 249–256. https://doi.org/10.1016/j.renene.2005.08.020.

[8]   Jones, B. R., Crossley, W. A., and Lyrintzis, A. S., "Aerodynamic and aeroacoustic optimization of rotorcraft airfoils via a parallel genetic algorithm," *Journal of Aircraft*, Vol. 37, No. 6, 2000, pp. 1088–1096. https://doi.org/10.2514/2.2717.

[9]   Marten, D., Wendler, J., Pechlivanoglou, G., Nayeri, C. N., and Paschereit, C. O., "QBLADE: an open source tool for design and simulation of horizontal and vertical axis wind turbines," *International Journal of Emerging Technology and Advanced Engineering*, Vol. 3, No. 3, 2013, pp. 264–269. https://doi.org/10.1115/GT2016-57184.

[10] van Rooij, R. P. J. O. M., "Modification of the boundary layer calculation in RFOIL for improved airfoil stall prediction," Delft University of Technology Report IW-96087R, 1996.

[11] Ramanujam, G., and Özdemir, H., "Improving Airfoil Lift Prediction," AIAA Paper 2017-1999, 2017. https://doi.org/10.2514/6.2017-1999.

[12] Johnson, F. T., Tinoco, E. N., and Yu, N. J., "Thirty Years Of Development And Application Of CFD At Boeing Commercial Airplanes, Seattle," *Computers and Fluids*, 2005, pp. 115–1151. https://doi.org/10.1016/j.compfluid.2004.06.005.

[13] Drela, M., and Giles, M. B., "Viscous-Inviscid Analysis of Transonic and Low Reynolds Number Airfoils," *AIAA Journal*, Vol. 25, No. 10, 1987, pp. 1347–1355. https://doi.org/10.2514/3.9789.

[14] Giles, M. B., and Drela, M., "Two-Dimensional Transonic Aerodynamic Design Method," *AIAA Journal*, Vol. 25, No. 9, 1987, pp. 1199–1206. https://doi.org/10.2514/3.9768.

[15] Drela, M., and Giles, M., "ISES: A Two-Dimensional Viscous Aerodynamic Design and Analysis Code," AIAA Paper 87-0424, 1987. https://doi.org/10.2514/6.1987-424.

[16] Bauer, F., Garabedian, P., Korn, D., and Jameson, A., "Supercritical Wing Sections II," *Lecture Notes in Economics and Mathematical Systems*, Vol. 108, Springer-Verlag Berlin Heidelberg New York, 1975. https://doi.org/10.1007/978-3-642-48912-9.

[17] Eppler, R., and Somers, D. M., "A Computer Program for the Design and Analysis of Low-Speed Airfoils," NASA Technical Memorandum 80210, 1980.

[18] Eppler, R., and Somers, D. M., "Supplement to: A Computer Program for the Design and Analysis of Low-Speed Airfoils," NASA Technical Memorandum 81862, 1980.

[19] Melnik, R., Brook, J., and Mead, H., "GRUMFOIL: A Computer Code for the Computation of Viscous Transonic Flow over Airfoils," AIAA Paper 87-0414, 1987. https://doi.org/10.2514/6.1987-414.

[20] Fidkowski, K. J., "mfoil," , 2021. URL http://websites.umich.edu/~kfid/codes.html, accessed: 2021-10-01.

[21] MATLAB, *version 7.10.0 (R2021b)*, The MathWorks Inc., Natick, Massachusetts, 2021.

[22] Drela, M., *Flight Vehicle Aerodynamics*, MIT Press, Cambridge, MA, 2014.

[23] Drela, M., "Integral boundary layer formulation for blunt trailing edges," AIAA Paper 89-2166-CP, 1989. https://doi.org/10.2514/6.1989-2166.

[24] Smith, A., and Gamberoni, N., "Transition, Pressure Gradient, and Stability Theory," Douglas Aircraft Company Report ES 26388, 1956.

[25] Goldstein, S., "On Laminar Boundary-Layer Flow Near a Position of Separation," *The Quarterly Journal of Mechanics and Applied Mathematics*, Vol. 1, 1948, pp. 43–69. https://doi.org/10.1093/qjmam/1.1.43.

[26] Shapiro, A. H., *The Dynamics and Thermodynamics of Compressible Fluid Flow, Volume I*, John Wiley & Sons, 1953.

[27] Squire, H., and Young, A., "The Calculation of the Profile Drag of Aerofoils," R.A.E. Report 1838, November 1937.